

# Complex superlattice unit cell designs for reduced thermal conductivity

E. S. Landry

*Department of Mechanical Engineering, Carnegie Mellon University, Pittsburgh, Pennsylvania 15213, USA*

M. I. Hussein

*Department of Aerospace Engineering Sciences, University of Colorado at Boulder, Boulder, Colorado 80309, USA*

A. J. H. McGaughey\*

*Department of Mechanical Engineering, Carnegie Mellon University, Pittsburgh, Pennsylvania 15213, USA*

(Received 8 February 2008; published 8 May 2008)

The suitability of the Green–Kubo method for predicting the thermal conductivity of nanocomposites is assessed by studying model Lennard–Jones superlattices. Good agreement is found when comparing the predicted cross-plane thermal conductivities to independent predictions from the direct method. The link between the superlattice unit cell design and the thermal conductivity tensor is then explored. We find that complex, multilayered unit cell designs can reduce the cross-plane thermal conductivity by 17% compared to the minimum value predicted for superlattices with only two layers in the unit cell. These results suggest new directions that can be explored for reducing thermal conductivity, which is desirable in applications such as designing materials for thermoelectric energy conversion.

DOI: [10.1103/PhysRevB.77.184302](https://doi.org/10.1103/PhysRevB.77.184302)

PACS number(s): 63.22.Np, 65.40.–b, 68.65.Cd

## I. INTRODUCTION

### A. Superlattice thermal conductivity

Superlattices are periodic, nanocomposite structures containing alternating material layers with thicknesses as small as a few nanometers.<sup>1–8</sup> These structures have traditionally been designed for control of electron transport. The thermal transport by phonons, however, can also be controlled through the proper design of the superlattice unit cell. The superlattice thermal conductivity tensor is anisotropic, with the in-plane thermal conductivity  $k_{IP}$  often being several factors greater than the cross-plane value  $k_{CP}$ .<sup>9–11</sup> This characteristic may lead to the use of superlattices in directional heat transfer applications (e.g., in electronics) where a material that can simultaneously insulate in one direction and channel heat in another is desired. Superlattices also have the potential to increase the efficiency of thermoelectric energy conversion devices. This is because  $k_{CP}$  can be reduced while maintaining good electron transport properties, resulting in high values of the thermoelectric figure of merit.<sup>12,13</sup>

The thermal properties of typical semiconductor superlattices (e.g., Si/Si<sub>1-x</sub>Ge<sub>x</sub>, GaAs/AlAs, and Bi<sub>2</sub>Te<sub>3</sub>/Sb<sub>2</sub>Te<sub>3</sub>) have been experimentally characterized.<sup>1–8</sup> Some studies have found  $k_{CP}$  to be less than the thermal conductivity of an alloy of similar composition.<sup>1–3,5,6,8</sup> In some of these cases, the reduction below the alloy thermal conductivity is due to defects and dislocations that result from the strain associated with the lattice mismatch.<sup>14,15</sup> Reductions below the alloy thermal conductivity have also been observed, however, for superlattices without significant defects or dislocations.<sup>1,6,8,15</sup> The effect of the superlattice period length on the experimentally observed  $k_{CP}$  is conflicting. Some studies have found that  $k_{CP}$  initially decreases with increasing period length until a minimum is reached, beyond which  $k_{CP}$  increases.<sup>2,3,8</sup> Others have observed that  $k_{CP}$  monotonically increases with increasing period length.<sup>1,7</sup> Experimental studies of Si/Ge

superlattices<sup>9</sup> and layered WSe<sub>2</sub> crystals<sup>10,11</sup> have reported  $k_{IP}/k_{CP}$  ratios of  $\sim 5$ – $6$  and  $\sim 30$ .

Lattice dynamics calculations<sup>16–24</sup> and molecular dynamics (MD) simulations<sup>11,25–30</sup> have been applied to investigate the experimental trends. Traditional lattice dynamics calculations require the assumption of coherent phonon transport. This assumption is only valid when the superlattice period length is not larger than the phonon mean free path. Lattice dynamics calculations performed under this assumption have been used to explain the trend of decreasing  $k_{CP}$  with increasing period length that is sometimes observed for small-period superlattices.<sup>19,21,22,24</sup> This trend is due to the formation of minibands (i.e., frequency gaps) in the phonon dispersion and reductions in the average phonon group velocity as the superlattice period length increases. Most of the traditional lattice dynamics-based approaches make the additional assumption that all phonon modes have the same relaxation time [i.e., the constant relaxation time approximation (CRTA)].<sup>19–24</sup> Broido and Reinecke<sup>18</sup> used an anharmonic lattice dynamics model to obtain the mode-specific relaxation times, finding a thermal conductivity trend similar to that obtained under the CRTA. They note, however, that the agreement between the trends is fortuitous and due to a cancellation of errors in the CRTA approach. When the superlattice period length exceeds the phonon mean free path, the phonon transport is incoherent (i.e., phonons scatter at the superlattice interfaces and the phonon properties are distinct within each layer). In this regime, the mechanism of  $k_{CP}$  reduction is phonon scattering at the interfaces. Therefore,  $k_{CP}$  increases with increasing period length due to decreasing interface density. Simkin and Mahan<sup>16</sup> incorporated the effects of incoherent phonon transport in lattice dynamics calculations by giving the phonons a finite mean free path. This task was accomplished through the addition of an imaginary component to the wave vector. The resulting model predicted a minimum in  $k_{CP}$ , corresponding to the period length where phonon transport tran-

sitions between the coherent and incoherent regimes. Yang and Chen<sup>17</sup> later expanded this model by adding a second imaginary component to the wave vector to account for diffuse phonon scattering at the interfaces. Good agreement with the experimental trends for GaAs/AlAs superlattices was obtained.

Chen *et al.*<sup>26</sup> applied MD to model Lennard-Jones (LJ) superlattices in order to examine the conditions required to produce a minimum  $k_{CP}$ . It was found that a minimum exists when there is no lattice mismatch, but when the species were given a lattice mismatch of 4%,  $k_{CP}$  monotonically increased with increasing period length. Daly *et al.*<sup>27</sup> and Imamura *et al.*<sup>28</sup> predicted the effect of interface roughness on the minimum  $k_{CP}$  for model GaAs/AlAs superlattices. Both groups found that the addition of rough interfaces decreased  $k_{CP}$  and removed the minimum that they observed for superlattices with perfect interfaces. Daly *et al.*<sup>27,31</sup> also predicted reduced anisotropy of the thermal conductivity tensor for superlattices with rough interfaces.

### B. Molecular dynamics prediction of the thermal conductivity

In a MD simulation, the Newtonian equations of motion are used to predict the time history of the positions and velocities of a set of atoms. Such simulations are an ideal tool for analyzing thermal transport in superlattices because, unlike lattice dynamics-based approaches, no assumptions about the nature of phonon transport (e.g., the CRTA) are required. The two most common methods to predict the thermal conductivity by using MD are the direct method and the Green–Kubo method. Schelling *et al.*<sup>32</sup> provided an in-depth comparison between these two methods by predicting the thermal conductivity of crystalline silicon. They found that the predictions agree with each other to within the measurement uncertainties. No comprehensive comparison between the thermal conductivity prediction methods has been reported for nanocomposites such as superlattices. The Green–Kubo method has advantages over the direct method in that it (i) predicts the full thermal conductivity tensor (i.e., both  $k_{IP}$  and  $k_{CP}$ ) from one simulation, and (ii) offers additional data for analysis (e.g., the heat current autocorrelation function). The direct method, however, has been used more extensively than the Green–Kubo method for predicting the thermal conductivity of superlattices. This fact may simply be related to the intuitive nature of the direct method approach, but the need for a quantitative comparison between the two methods for this class of materials is clear.

### C. Overview

The two main objectives of this work are to (i) assess the suitability of the Green–Kubo method for predicting the thermal conductivity of nanocomposites and (ii) explore the link between the superlattice unit cell design and the thermal conductivity tensor, and, in doing so, explore new concepts for the unit cell design. The first objective is accomplished by comparing the Green–Kubo  $k_{CP}$  predictions for model LJ superlattices to independent predictions obtained by using the direct method. Both methods are discussed in detail in Secs. III and IV, and the results of the comparison are presented in

Sec. V. With a prediction methodology established, in Sec. VI, we predict the full thermal conductivity tensor for superlattices with two layers of equal thickness in the unit cell. With the goal of minimizing  $k_{CP}$ , we then examine complex unit cell designs consisting of more than two layers in the unit cell and show that significant reductions ( $\sim 17\%$ ) in  $k_{CP}$  are possible over the superlattices with only two layers in the unit cell.

## II. SUPERLATTICE MODEL AND SIMULATION LOGISTICS

In this study, the superlattices are built on face-centered-cubic lattice sites and are comprised of two species, *A* and *B*. The atomic interactions are modeled by using the LJ 12-6 potential,

$$\phi_{ij}(r_{ij}) = 4\epsilon_{LJ} \left[ \left( \frac{\sigma_{LJ}}{r_{ij}} \right)^{12} - \left( \frac{\sigma_{LJ}}{r_{ij}} \right)^6 \right], \quad (1)$$

where  $r_{ij}$  is the distance between atoms *i* and *j*, and  $\sigma_{LJ}$  and  $\epsilon_{LJ}$  are the zero-energy pair separation distance and potential well depth. We choose the  $\sigma_{LJ}$  and  $\epsilon_{LJ}$  values for argon, which are  $3.40 \times 10^{-10}$  m and  $1.67 \times 10^{-21}$  J, respectively.<sup>33</sup> The mass scale  $m_{LJ}$  is the mass of one argon atom,  $6.63 \times 10^{-26}$  kg. The simple form of the LJ potential allows for fast simulations, and for the elucidation of phenomena and development of analysis techniques that would not be possible in more complicated systems. The two species have a mass ratio  $R_m$  of

$$R_m \equiv \frac{m_B}{m_A}. \quad (2)$$

Here,  $m_A$  is  $m_{LJ}$  in all cases, and the value of  $m_B$  is varied to obtain a desired  $R_m$ . Here, we examine mass ratios of two and five, spanning a typical range for real superlattices (e.g., the mass ratio between germanium and silicon is 2.6). Apart from this mass difference, the species are identical, allowing for the use of previously determined zero-pressure lattice constants.<sup>34</sup> Also, because there is no lattice mismatch between the species, the superlattices have zero strain.

Both the mass ratio and unit cell design must be specified to define a particular superlattice. The unit cell is specified by using the format:  $L_{A,1} \times L_{B,1} \times L_{A,2} \times L_{B,2}$ , where  $L_A$  and  $L_B$  are the thicknesses of individual layers in monolayers. For example, the unit cell for the  $1 \times 1 \times 2 \times 2$  superlattice has a repeating sequence of one monolayer of *A*, one monolayer of *B*, two monolayers of *A*, and two monolayers of *B*. The total period length for this case is then  $L = 1 + 1 + 2 + 2 = 6$  monolayers. The  $3 \times 3$  superlattice is shown in Fig. 1. In our coordinate system, the *x* and *y* directions indicate the directions parallel to the layers and are labeled as the in-plane directions. The *z* direction indicates the direction perpendicular to the layers and is labeled as the cross-plane direction.

All thermal conductivity predictions are made at zero-pressure and a temperature of 40 K, a moderate temperature for LJ argon (melting occurs at 87 K). The zero-pressure lattice constant, *a*, at this temperature is  $5.3697 \text{ \AA}$ .<sup>34</sup> Note

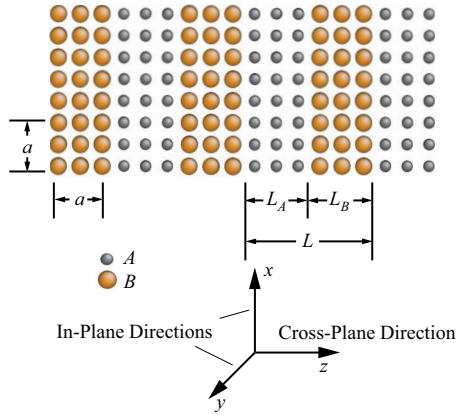


FIG. 1. (Color online) Superlattice with cross-plane and in-plane directions labeled. This superlattice is the  $3 \times 3$  structure, which indicates  $L_A = L_B = 3$  monolayers and a total period length of  $L = 6$  monolayers.

that the lattice constant corresponds to the thickness of two monolayers (see Fig. 1).

The Newtonian equations of motion are integrated by using the velocity Verlet algorithm. A truncated and shifted cutoff scheme is used with a cutoff radius of  $2.5\sigma_{LJ}$  and a time step of  $0.002\sqrt{\sigma_{LJ}^2 m_{LJ} / \epsilon_{LJ}}$  (4.285 fs). The number of atoms in the simulation cell ranges from 1152 to 9152 and is dependent on the thermal conductivity prediction method and the particular superlattice being examined. Further details related to the MD simulations and the thermal conductivity prediction methods are provided in Secs. III and IV.

### III. GREEN-KUBO METHOD

#### A. Formulation and heat current definitions

The Green-Kubo method relates the equilibrium fluctuations of the heat current vector  $\mathbf{S}$  to the thermal conductivity  $k$  via the fluctuation-dissipation theorem. The superlattice thermal conductivity in the  $l$ th direction (either the cross-plane or in-plane direction) is given by<sup>35</sup>

$$k_l = \frac{1}{k_B V T^2} \int_0^\infty \langle S_l(t) S_l(0) \rangle dt, \quad (3)$$

where  $t$  is time,  $V$  and  $T$  are the system volume and temperature, and  $S_l$  and  $\langle S_l(t) S_l(0) \rangle$  are the  $l$ th components of the heat current vector and the heat current autocorrelation function (HCACF).

There are multiple ways to define the heat current vector in a solid.<sup>36–38</sup> The most commonly used definition is

$$\mathbf{S}_1 = \frac{d}{dt} \sum_i \mathbf{r}_i E_i, \quad (4)$$

where  $\mathbf{r}_i$  and  $E_i$  are the position vector and energy of atom  $i$ , and the summation is over all of the atoms in the system. In a solid, where there is no net atomic motion, the heat flux can also be written by using the equilibrium positions ( $\mathbf{r}_{i,o}$ ) as

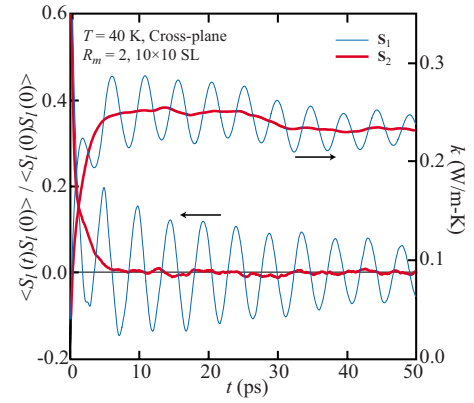


FIG. 2. (Color online) The Green-Kubo HCACF and its integral (the converged value is proportional to the thermal conductivity) plotted versus the correlation time for the  $R_m = 2$ ,  $10 \times 10$  superlattice in the cross-plane direction. The heat current has been calculated using the instantaneous [ $\mathbf{S}_1$ , Eq. (6)] and equilibrium [ $\mathbf{S}_2$ , Eq. (7)] atomic positions. The HCACFs are normalized by their initial values.

$$\mathbf{S}_2 = \frac{d}{dt} \sum_i \mathbf{r}_{i,o} E_i. \quad (5)$$

For a pair potential, Eqs. (4) and (5) can be recast as

$$\mathbf{S}_1 = \sum_i E_i \mathbf{v}_i + \frac{1}{2} \sum_i \sum_{j>i} (\mathbf{F}_{ij} \cdot \mathbf{v}_i) \mathbf{r}_{ij}, \quad (6)$$

$$\mathbf{S}_2 = \frac{1}{2} \sum_i \sum_{j>i} (\mathbf{F}_{ij} \cdot \mathbf{v}_i) \mathbf{r}_{ij,o}, \quad (7)$$

where  $\mathbf{v}_i$  is the velocity of atom  $i$ ,  $\mathbf{F}_{ij}$  is the force exerted by atom  $j$  on atom  $i$ , and  $\mathbf{r}_{ij}$  and  $\mathbf{r}_{ij,o}$  are the instantaneous and equilibrium interparticle separation vectors between atoms  $i$  and  $j$ .

For all of our Green-Kubo thermal conductivity predictions, data are collected from simulations run in the  $NVE$  (constant mass, volume, and energy) ensemble for a period of  $1 \times 10^6$  time steps after an equilibration period of  $5 \times 10^5$  time steps. During the data collection period, the heat current is calculated every five time steps. A correlation length of  $5 \times 10^4$  time steps with  $2 \times 10^5$  time origins is used in the calculation of the HCACF. In order to properly sample the phase space, the HCACFs from five independent simulations, where each has random initial velocities, are averaged. From this averaged HCACF, the thermal conductivity is obtained by using Eq. (3).

The two definitions of the heat current are compared in Fig. 2 in a plot of the HCACF and its integral (the converged value is proportional to the thermal conductivity) for the  $R_m = 2$ ,  $10 \times 10$  superlattice in the cross-plane direction. The integrals of the HCACFs converge at the same value. The instantaneous values of the integrals of the HCACFs are different, however, due to the large oscillations in the HCACF, which are obtained using the  $\mathbf{S}_1$  heat current definition. Similar oscillations have been observed in the HCACFs of many different material systems.<sup>30,39–44</sup> As discussed in the Appen-

dix, these oscillations are caused by specific zero-wave-vector optical phonon modes and are related to the first summation in Eq. (6). The oscillations in the HCACF make accurate specification of the thermal conductivity difficult. Therefore, we will use  $S_2$  to predict the thermal conductivity. An added benefit of using this definition is that it does not require the calculation of the energy of each atom, thus reducing the computation time.

### B. Green–Kubo cell-size effect

In the Green–Kubo method, the thermal conductivity may depend on the size of the simulation cell if there are not enough phonon modes to accurately reproduce the phonon scattering in the associated bulk material. This size dependence is removed by increasing the simulation cell size until the thermal conductivity reaches a size-independent value. We find that the cross-plane dimensions required to remove the simulation cell-size effect are superlattice dependent. For superlattices with  $L \leq 10$ , eight periods are required. For the  $L=20$  and  $L=40$  superlattices, four and two periods are required. The required length of the simulation cell is smaller for the small-period superlattices than the large-period superlattices because there is more phonon scattering due to the larger number of interfaces. In all cases, the required in-plane area is six unit cells by six unit cells. These in-plane dimensions are larger than the four unit cells by four unit cells often reported to remove the Green–Kubo simulation-cell-size effects in LJ argon.<sup>45,46</sup> We attribute this difference to our noncubic simulation cells.

### C. $5 \times 5$ superlattice thermal conductivity prediction

To illustrate the challenges encountered when applying the Green–Kubo method to predict the superlattice thermal conductivity, we focus on the  $5 \times 5$  superlattice. The HCACF [calculated by using the definition of the heat current given by Eq. (7)] and its integral are shown in Fig. 3 for the  $R_m=2$ ,  $5 \times 5$  and  $R_m=5$ ,  $5 \times 5$  superlattices. For both mass ratios, the in-plane HCACF monotonically decays in two stages. The first stage (before  $\sim 5$  ps in both cases) is a rapid decay of the HCACF resulting from the motion of each atom sampling its local environment.<sup>46</sup> The second stage is a slower decay to zero, which can be attributed to phonon scattering.<sup>45,46</sup> Both in-plane HCACFs appear to decay to zero after 20–30 ps, but their integrals do not converge until a correlation time of approximately 50 ps [see the insets in Figs. 3(a) and 3(b)]. The in-plane thermal conductivity is specified on a case-by-case basis by averaging the integral of the HCACF over the region where it has converged.

For the cross-plane direction, the result for the  $R_m=2$  case is qualitatively similar to that for the in-plane direction. The  $R_m=5$  case, however, exhibits different behaviors. The HCACF is negative between correlation times of 1 and 5 ps, with a minimum at 2 ps. We note that this minimum is difficult to observe when using the  $S_1$  heat current definition because of the strong oscillations (see Fig. 2) that dominate the shape of the HCACF. We find that for the  $L_A=L_B$  superlattices, the time at the HCACF minimum increases linearly with the layer thicknesses. By plotting the layer thickness

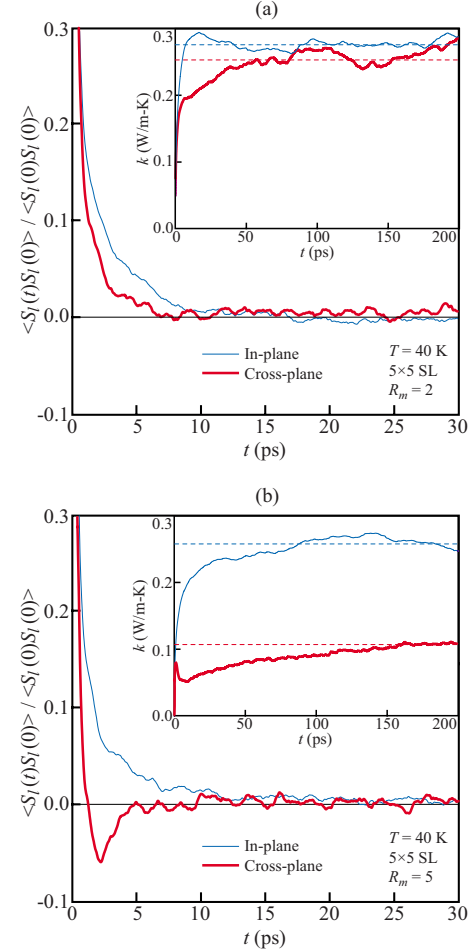


FIG. 3. (Color online) In-plane and cross-plane HCACFs for the (a)  $R_m=2$ ,  $5 \times 5$  and (b)  $R_m=5$ ,  $5 \times 5$  superlattices. The HCACFs have been normalized by their initial values. The integrals of the HCACFs (the thermal conductivity) and their converged values (dashed lines) are shown in the figure insets.

against the time at the minimum, a velocity can be extracted from the slope. This velocity is 520 m/s, approximately 70% of the average of the sound speeds (estimated as the average of the three cross-plane acoustic phonon group velocities in the limit of zero wave vector) of species  $A$  and  $B$ . This agreement suggests that the negative correlation in the HCACF is due to energy reflection at the superlattice interfaces. Because the two species in the  $R_m=2$  superlattices have a smaller acoustic mismatch (defined as  $\rho_B c_B / \rho_A c_A$ , where  $\rho$  is the density and  $c$  is the sound speed<sup>47</sup>) than the  $R_m=5$  superlattices, the negative correlation caused by energy reflection at the interfaces is not as strong.

As with the in-plane direction, the converged value of the integral of the cross-plane HCACF is specified on a case-by-case basis. We note, however, that determining the converged region of the cross-plane HCACF integral is not a trivial task. For some of the complex unit cell designs that are described in Sec. VI C, it is not possible to determine a region of convergence in the integral of the cross-plane HCACF, even after increasing the autocorrelation length and the number of independent simulations. For structures where we can identify a region of convergence (e.g.,  $L_A=L_B$  superlattices),

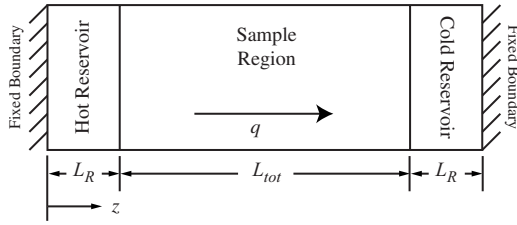


FIG. 4. Schematic of the simulation cell used in the direct method.

we estimate the thermal conductivity prediction uncertainty to be  $\pm 20\%$  in both directions.

We note that in previous studies by members of this group, a decomposition procedure was used to fit the HCACF to a sum of algebraic functions to remove some of the ambiguity encountered when directly specifying the HCACF integral.<sup>30,40,43,45</sup> Similar decomposition procedures have been successfully applied by others.<sup>39,48</sup> When applied to the superlattices considered here, however, a good fit between the decomposition function and the HCACF was not always possible. One reason for this result is the region of negative correlation that is observed in the cross-plane direction when  $R_m=5$ . We believe that this region of negative correlation was also the cause of our inability to decompose the cross-plane HCACF for the  $R_m=5$  and  $R_m=10$  monolayer superlattices examined in a previous study.<sup>30</sup> We note that a similar negative region in the HCACF is observed in amorphous LJ argon, a material for which the decomposition procedure was also unsuccessful.<sup>34,45</sup>

In Sec. IV, we apply the direct method to carry out independent thermal conductivity prediction calculations. These calculations are subsequently used to assess the performance of the Green–Kubo method.

#### IV. DIRECT METHOD

##### A. Background

The direct method is a nonequilibrium, steady-state approach based on the Fourier law for predicting the thermal conductivity.<sup>32,36</sup> The thermal conductivity is found by imposing a heat flux  $q$  across the sample and measuring the resulting temperature gradient. Alternatively, a temperature gradient can be imposed across the sample, and the resulting heat flux can be measured. Lukes *et al.*<sup>49</sup> noted that long simulation times are required to obtain convergence of the heat flux value when using the imposed temperature gradient method, and therefore, we use the imposed heat flux method. As mentioned in Sec. I, the direct method can only predict the thermal conductivity in one direction per simulation. Here, we only predict the cross-plane thermal conductivity because very large simulation cell sizes would be required to predict the in-plane value.

A schematic of the direct method simulation cell is shown in Fig. 4. The system consists of a superlattice sample bordered by hot and cold reservoirs and fixed boundaries in the  $z$  direction. Periodic boundary conditions are imposed in the in-plane directions. This simulation cell setup was selected

TABLE I. Effects of reservoir thickness, in-plane dimensions, and imposed heat flux on the direct method cross-plane thermal conductivity prediction for the  $R_m=2, 5 \times 5$  superlattice. The maximum uncertainty in the thermal conductivity prediction is estimated to be  $\pm 10\%$ .

	$q$ (GW/m <sup>2</sup> )	IP Dimensions (UC $\times$ UC)	$L_R$ (monolayers)	$k_{CP}$ (W/m K)
A	35.6	4 $\times$ 4	4	0.235
B	35.6	4 $\times$ 4	8	0.248
C	35.6	4 $\times$ 4	12	0.233
D	35.6	4 $\times$ 4	16	0.216
E	35.6	5 $\times$ 5	4	0.217
F	35.6	6 $\times$ 6	4	0.225
G	28.5	4 $\times$ 4	4	0.222
H	32.1	4 $\times$ 4	4	0.225
I	39.2	4 $\times$ 4	4	0.235
J	42.8	4 $\times$ 4	4	0.222

over a system that uses periodic boundary conditions in all three directions (see Ref. 32 for details) because larger samples can be studied with the same total number of atoms. Each of the fixed boundary regions contain four monolayers of fixed atoms in order to prevent the sublimation of the reservoir atoms. The thickness of the fixed boundary region is greater than the interatomic potential cutoff radius and should have no effect on the predicted thermal conductivity (i.e., the atoms in the reservoirs “see” an infinite boundary region). The reservoirs are comprised of atoms of the same species as the sample atoms that immediately border the reservoir.

In Table I, the effects of the reservoir length (simulations labeled A–D) and the in-plane dimensions (simulations labeled A, E, and F) on the predicted cross-plane thermal conductivity are shown for the  $R_m=2, 5 \times 5$  superlattice. The reservoir length  $L_R$  has negligible effect on the predicted cross-plane thermal conductivity (details related to the thermal conductivity prediction will be provided in Secs. IV B–IV D) when it is greater than or equal to four monolayers. The predicted cross-plane thermal conductivity is independent of the in-plane dimensions when they are greater than or equal to four unit cells by four unit cells. All of the thermal conductivity predictions in Table I are within  $\pm 10\%$  of the value predicted for simulation A. Therefore, we believe that our prediction uncertainty is a maximum of  $\pm 10\%$ . We note that we have found that direct method thermal conductivity predictions for silicon/germanium superlattices are more sensitive to the reservoir composition and size than the LJ superlattices.<sup>50,51</sup> In our view, this higher sensitivity is a result of the silicon/germanium superlattices having thermal conductivities that are an order of magnitude higher than the LJ superlattices.

##### B. Imposing the heat flux

The heat flux across the sample is generated by adding a constant amount of kinetic energy  $\Delta E_k$  to the hot reservoir

and by removing  $\Delta E_k$  from the cold reservoir at every time step using the method described by Ikeshoji and Hafskjold.<sup>52</sup> The heat flux generated with this scheme is

$$q = \frac{\Delta E_k}{A_c \Delta t}, \quad (8)$$

where  $A_c$  is the cross-sectional area of the sample.

The value of the heat flux should be chosen so that the temperature drop  $\Delta T$  across the sample is large enough to accurately specify the temperature gradient. It should not be too large, however, to introduce nonlinear temperature profiles due to the temperature dependence of the thermal conductivity. We define the temperature drop across the sample to be

$$\Delta T = -L_{\text{tot}} \frac{\partial T}{\partial z}, \quad (9)$$

where  $L_{\text{tot}}$  is the total sample length and  $\partial T/\partial z$  is the temperature gradient (details related to the specification of the temperature gradient are provided in Sec. IV C). Heat flux values that produce temperature drops of approximately 10 K lead to temperature gradients that can be accurately specified without introducing nonlinear effects (see the independence of the cross-plane thermal conductivity on the heat flux in the simulations labeled A, G, H, I, and J in Table I for the  $R_m=2, 5 \times 5$  superlattice). In this work, the thermal conductivity predictions are made using heat flux values that result in temperature drops of  $10 \pm 1$  K across the sample.

### C. Data collection and analysis

In order to quickly achieve a steady temperature profile (a requirement for the use of the Fourier law), we impose an initially linear temperature profile across the sample. The initial temperature profile has a total temperature drop of 10 K, and the midpoint of the sample is set to a temperature of 40 K. This profile is realized by scaling the atomic velocities in each layer for 25 000 time steps. The heat flux is then applied across the system. From this point, a period of  $1 \times 10^6/2 \times 10^6$  million time steps is allowed for the  $R_m = 2/R_m = 5$  superlattices to reach steady-state conditions. A longer time is required for the  $R_m = 5$  structures because they have a larger thermal diffusivity, a quantity that indicates how quickly a material adjusts to changes in its thermal environment.<sup>53</sup> Once the system has reached steady state, data are collected for the thermal conductivity prediction over an additional  $2 \times 10^6$  time steps.

The temperature of each atomic layer is found by averaging over the data collection period. A least-squares regression analysis is used to calculate the temperature gradient, which is then used to predict the thermal conductivity by using the Fourier law. We note that the temperature gradient could also be specified as the difference between the temperatures at the ends of the sample region divided by the sample length.<sup>54</sup> The maximum difference between the thermal conductivity predicted using these two methods of specifying the temperature gradient is 7%. This maximum occurs for the  $R_m = 5, 20 \times 20$  superlattice with two periods in the sample

because this structure has appreciable temperature drops (approximately 1.3 K) at the internal interfaces. For the smaller period superlattices (and especially for the  $R_m = 2$  structures), significant temperature drops at the interfaces are not observed, and therefore, the thermal conductivities obtained by using both methods of specifying the temperature gradient are in better agreement. Because more data is used to specify the temperature gradient by using the least-squares regression analysis, we apply this method as it will be less susceptible to statistical fluctuations.

### D. Direct method cell-size effect

As with the Green–Kubo method, simulation cell-size effects are present in the direct method due to simulation cells that are too small to capture the true nature of the bulk phonon scattering. In the Green–Kubo method, the phonon scattering is best thought of in terms of relaxation times rather than mean free paths because the simulation cell size is not large enough to allow for the formation of spatially localized wave packets that can propagate.<sup>36,55</sup> Even though long wavelength modes do not exist in the Green–Kubo simulation cell, the simulation cell can be made large enough to support a spectrum of phonon modes that accurately reproduce the phonon scattering in an infinite-sized sample.

In the direct method, however, the simulation cell length  $L_{\text{tot}}$  (see Fig. 4) is long enough to allow phonons to propagate. Because  $L_{\text{tot}}$  is on the order of the bulk phonon mean free path, significant phonon scattering will occur at the boundaries between the reservoirs and the sample, and phonons can potentially travel from the hot reservoir to the cold reservoir without scattering (i.e., ballistic transport). Both these effects lead to a dependence between the predicted thermal conductivity and the sample length. This dependence can be removed in one of two ways. First, the simulation cell length can be increased until size-independent results are obtained. Second, the results for several systems can be extrapolated to the thermal conductivity of an infinite system by using the method described by Schelling *et al.*<sup>32</sup> In the second method, it is assumed that the inverse of the effective phonon mean free path  $\Lambda_{\text{eff}}$  can be obtained through the Matthiessen rule<sup>56</sup> by adding the inverses of the mean free path in an infinite (i.e., bulk) system  $\Lambda_{\infty}$  and the effect of the finite system, i.e.,

$$\frac{1}{\Lambda_{\text{eff}}} = \frac{1}{\Lambda_{\infty}} + \frac{2}{L_{\text{tot}}}. \quad (10)$$

The factor of 2 in the numerator of the boundary scattering term comes from the fact that, on average, a phonon will travel a distance of  $L_{\text{tot}}/2$  before scattering at the boundary. In the work of Schelling *et al.*,<sup>32</sup> a factor of 4 is used due to differences in their simulation cell setup. From the kinetic theory expression for thermal conductivity,<sup>33</sup>

$$k = \rho C_v c \Lambda / 3, \quad (11)$$

where  $C_v$  is the constant volume specific heat, Eq. (10) can be restated as

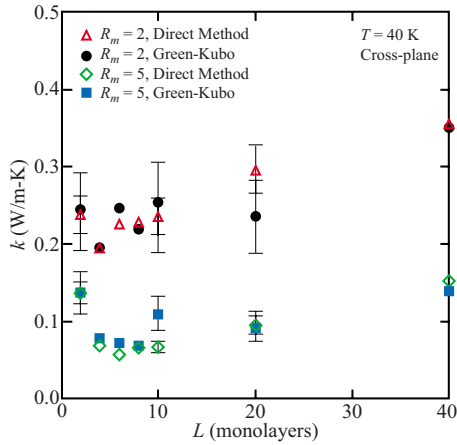


FIG. 5. (Color online) Comparison between the cross-plane thermal conductivity predictions obtained by the Green-Kubo and direct methods for the  $R_m=2$  and  $R_m=5$ ,  $L_A=L_B$  superlattices. The error bars have been included for a selection of the results.

$$\frac{1}{k} = \frac{3}{\rho C_v c} \left( \frac{1}{\Lambda_{\text{eff}}} - \frac{2}{L_{\text{tot}}} \right). \quad (12)$$

This result suggests that the finite size effects can be removed by plotting  $1/k$  vs  $1/L_{\text{tot}}$  and extrapolating to an infinite system size ( $L_{\text{tot}} \rightarrow \infty$ ). Chen *et al.*<sup>26</sup> stated that the extrapolation method should be used for LJ superlattices periods with  $L \geq 16$  monolayers. For structures with  $L < 16$  monolayers, however, they indicated that the size effects are eliminated when the total sample length sample is greater than or equal to 256 monolayers. We have verified these claims and have used their suggestions. We note that these suggestions are generally not applicable for non-LJ superlattices.

## V. COMPARISON BETWEEN THE GREEN-KUBO AND DIRECT METHODS

The Green-Kubo and direct method predictions for the cross-plane thermal conductivity are shown together in Fig. 5 for the  $L_A=L_B$  superlattices. The error bars corresponding to the measurement uncertainties reported in Secs. III and IV are provided for several points. For all but one point ( $R_m=5$ ,  $5 \times 5$ ), the two sets of predictions are in agreement and neither method consistently underpredicts nor overpredicts the other. We therefore conclude that either the Green-Kubo method or direct method can be used to predict the thermal conductivity of  $L_A=L_B$  superlattices. As mentioned in Sec. III C, however, we encounter difficulties in obtaining convergence of the cross-plane HCACF integral for more complex unit cell designs (as discussed in Sec. VI C). Because of this difficulty and the fact that the prediction uncertainty is less for the direct method than the Green-Kubo method, we prefer to use the direct method for the cross-plane thermal conductivity predictions. All data reported in the remainder of this paper correspond to the direct method for the cross-plane and Green-Kubo methods for the in-plane thermal conductivity predictions (convergence of the

HCACF integral is always obtained for the in-plane direction).

## VI. THERMAL CONDUCTIVITY DESIGN SPACE

### A. Theoretical bounds on the thermal conductivity

The theoretical upper bound to the superlattice thermal conductivity design space is given by the diffuse limit, which is reached when the superlattice layer thicknesses are much greater than the phonon mean free paths of the bulk phases. The in-plane and cross-plane thermal conductivities at the diffuse limit,  $k_{\text{IP,diff}}$  and  $k_{\text{CP,diff}}$ , are

$$k_{\text{IP,diff}} = \frac{t_A k_A + t_B k_B}{t_A + t_B}, \quad (13)$$

$$k_{\text{CP,diff}} = \frac{t_A + t_B}{t_A k_A^{-1} + t_B k_B^{-1} + 2R_{A|B}}, \quad (14)$$

where  $k_A$  and  $k_B$  are the bulk species thermal conductivities, and  $R_{A|B}$  is the thermal resistance of an isolated  $A|B$  interface. The thermal conductivity of bulk species  $A$  at a temperature of 40 K was previously predicted using the Green-Kubo method to be 0.467 W/m K.<sup>34</sup> The thermal conductivity of bulk species  $B$  is  $R_m^{-1/2}$  times the value for species  $A$ . Because we are looking for an upper limit on the superlattice thermal conductivity, we assume for this calculation that  $R_{A|B}$  is negligible compared to the resistance of the individual layers.

A lower bound for the thermal conductivity of a crystalline solid is the alloy limit.<sup>15</sup> In some experimental studies, superlattice thermal conductivities below that of an alloy with similar composition have been measured.<sup>1,2,5,6,8</sup> As mentioned in Sec. I, however, it has been suggested that such results are related to point defects and dislocations generated by the strain associated with lattice mismatch between the superlattice species.<sup>14</sup> Because our superlattices have perfect interfaces and no lattice mismatch, we can see if a proper design of the superlattice unit cell alone can lead to thermal conductivities at or below the alloy limit. The alloy thermal conductivity  $k_{\text{alloy}}$  is predicted by using the Green-Kubo method and a 256-atom cubic simulation cell. The atoms are located at fcc lattice sites with masses randomly assigned according to a desired species ratio  $R_s$  given by

$$R_s \equiv \frac{N_A}{N} = \frac{N - N_B}{N}, \quad (15)$$

where  $N$  is the total number of atoms, and  $N_A$  and  $N_B$  are the number of atoms of species  $A$  and  $B$ . We will compare the superlattice thermal conductivity to the thermal conductivity of an alloy with the same species ratio (e.g., the  $L_A=L_B$  superlattices are compared to an alloy with  $R_s=0.5$ ).

Cahill *et al.*<sup>57</sup> proposed a model for a minimum thermal conductivity, which is reached when all phonons have a mean free path equal to half of their wavelength. This minimum thermal conductivity, which we refer to as the high scatter limit, corresponds to a system with no long range order. Not surprisingly, the thermal conductivities predicted

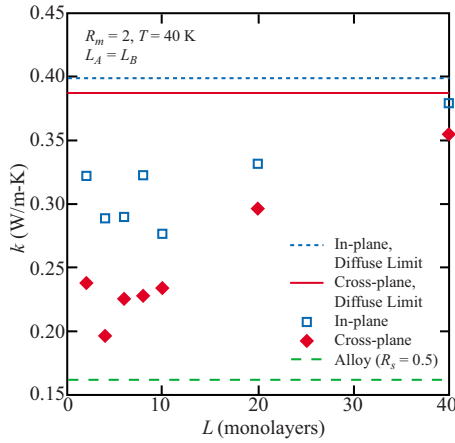


FIG. 6. (Color online) Thermal conductivity of the  $R_m=2$ ,  $L_A=L_B$  superlattices in the cross-plane and in-plane directions plotted as a function of total period length ( $L=L_A+L_B$ ). The thermal conductivity at the diffuse and alloy limits are also provided for comparison. The thermal conductivity at the high-scatter limit (not shown in figure) is 0.102 W/m K.

by this model are in agreement with experimentally measured thermal conductivities of amorphous materials.<sup>57</sup> Assuming isotropic and linear phonon dispersion, fully excited phonon modes (valid for the classical MD system), and harmonic specific heats, the thermal conductivity at the high-scatter limit  $k_{HS}$  is

$$k_{HS} = \frac{3}{2} \left( \frac{\pi}{6} \right)^{1/3} k_B n_v^{2/3} c, \quad (16)$$

where  $n_v$  is the atomic number density. Because the sound speed for the amorphous LJ phase is not available, we estimate it by scaling the average [100] sound speed by a factor of 0.8 (a typical value for the ratio of the amorphous to crystalline sound speeds for silicon and germanium<sup>57,58</sup>). We compare the superlattice thermal conductivity to the high-scatter limit by calculating the sound speed for a monatomic crystal that has the same mass density as the superlattice.

### B. $L_A=L_B$ superlattices

The predicted cross-plane and in-plane thermal conductivities for the  $R_m=2$ ,  $L_A=L_B$  superlattices are shown in Fig. 6. The superlattice thermal conductivities are between the alloy and the diffuse limits. The thermal conductivity at the high-scatter limit is 0.102 W/m K, a value that is below both the superlattice and alloy thermal conductivities. Starting from the diffuse limit, the cross-plane thermal conductivity initially decreases with decreasing period length due to increasing interface density, which is a behavior that is indicative of incoherent phonon transport. There is a minimum at a total period length of  $L=4$  monolayers, beyond which the cross-plane thermal conductivity increases with further decreases in the period length. This minimum indicates a transition from incoherent to coherent phonon transport. In order to examine the statistical significance of this minimum, ten independent simulations of the  $2 \times 2$  superlattice were run. The results indicate that the prediction is highly repeat-

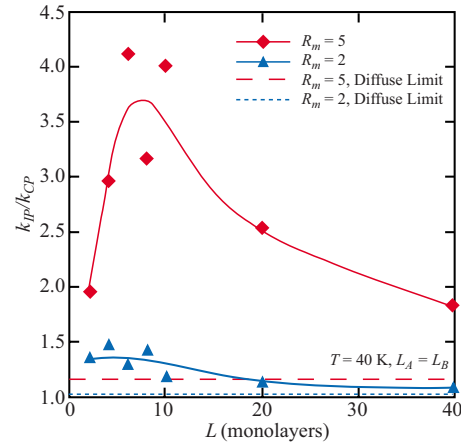


FIG. 7. (Color online) In-plane to cross-plane thermal conductivity ratio for the  $L_A=L_B$  superlattices plotted as a function of total period length ( $L=L_A+L_B$ ). Solid lines have been added to guide the eye.

able, with an average cross-plane thermal conductivity of 0.197 W/m K and a standard deviation of 4%. These results are in agreement with the predictions of Chen *et al.*,<sup>26</sup> who found that a minimum exists for LJ  $L_A=L_B$  superlattices when the species have no lattice mismatch and that the transition from incoherent to coherent phonon transport occurs when the phonon mean free path becomes greater than or equal to the superlattice period length. Therefore, based on our data, we estimate the phonon mean free path to be  $\sim 4-6$  monolayers. We note that a similar dependence between the cross-plane thermal conductivity and the total period length is observed for the  $R_m=5$ ,  $L_A=L_B$  superlattices (see Fig. 5). The minimum in the cross-plane thermal conductivity has been experimentally observed<sup>2,3,8</sup> and predicted by using lattice dynamics calculations<sup>16</sup> and MD simulations.<sup>26</sup>

The predicted in-plane to cross-plane thermal conductivity ratio is shown in Fig. 7 for the  $R_m=2$  and  $R_m=5$ ,  $L_A=L_B$  superlattices along with corresponding diffuse-limit values. The thermal conductivity ratio is always greater than the value at the diffuse limit. The maximum in-plane to cross-plane thermal conductivity ratios are  $\sim 1.4$  and  $\sim 3.6$  for the  $R_m=2$  and  $R_m=5$  superlattices, respectively, and occur for superlattices with total period lengths of four and six monolayers. These period lengths correspond to the region where the phonon transport transitions between the coherent and incoherent regimes.

Our thermal conductivity ratios are lower than values that are experimentally observed<sup>9</sup> and theoretically predicted<sup>17,27,31</sup> for superlattices with similar mass ratios. Yang *et al.*<sup>9</sup> experimentally measured a thermal conductivity ratio of five to six for a Si/Ge superlattice. By using a lattice dynamics model, Yang and Chen<sup>17</sup> predicted thermal conductivity ratios of five for GaAs/AlAs superlattices. Daly *et al.*<sup>27,31</sup> predicted thermal conductivity ratios of two to three for model GaAs/AlAs superlattices with perfect interfaces. The lack of strain within our superlattices (i.e., there is no lattice mismatch) may lead to the smaller thermal conductivity ratios. We note that the thermal conductivity ratios predicted here and measured<sup>9</sup> or predicted by others<sup>17,27,31</sup> are

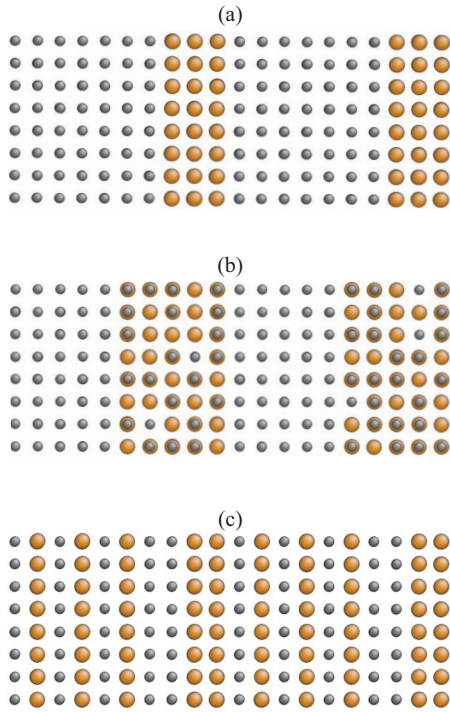


FIG. 8. (Color online) Sample superlattice unit cell designs: (a) a  $7 \times 3$  superlattice (one case in the  $L_A + L_B = 10$  series), (b) a superlattice with an alloy layer, and (c) complex design XI [i.e., the  $(1 \times 1)_3 \times 2 \times 2$  superlattice, see Table II].

well below the value of  $\sim 30$ , which is experimentally observed for layered  $\text{WSe}_2$  crystals.<sup>10,11</sup>

### C. Complex unit cell designs

In this section, we further explore the effect of unit cell design on the cross-plane thermal conductivity for the

$R_m = 2$  structures. We consider structures where  $L_A + L_B$  is equal to four or ten monolayers, two alloy superlattices, and unit cells with complex designs. Three of these designs are shown in Fig. 8. The two alloy superlattices have five layers of an alloy with  $R_s = 0.5$  and five layers of either  $A$  or  $B$ . We consider alloy superlattices because similar structures are currently used in application (e.g.,  $\text{Si}/\text{Si}_{1-x}\text{Ge}_x$  superlattices<sup>59</sup>). The complex unit cell designs and their labels are listed in Table II. The inclusion of unit cells with more than two layers of varying thicknesses was inspired by earlier work done in the area of phononic crystals.<sup>60</sup> Because the minimum cross-plane thermal conductivity for the  $L_A = L_B$  superlattices was observed for the  $2 \times 2$  superlattice (see Fig. 6), we focus on complex designs that have layer thicknesses of one, two, and three monolayers.

We consider two classes of complex unit cell designs. In the first class (complex designs I through III), the unit cell contains no ordered subcells and has a total period length that is greater than the phonon mean free path ( $\sim 4-6$  monolayers, see Sec. VI B). The phonon transport in these structures is thus incoherent and the cross-plane thermal conductivity may be reduced by phonon scattering at interfaces. In the second class (complex designs IV–XII), the unit cell is a  $1 \times 1$  or  $2 \times 2$  superlattice with disruptions spaced on the order of the phonon mean free path (e.g., the  $1 \times 1$  subcell in design VII is a disruption in what would otherwise be a  $2 \times 2$  superlattice). Because of phonon scattering at these disruptions, the phonon mean free paths and thermal conductivities may be below the values that would exist in the  $1 \times 1$  and  $2 \times 2$  superlattices. We note that there exists a third class of designs, in which the unit cell contains many layers with no ordered subcells but has a total period length less than or equal to the phonon mean free path. Within this class, the phonon transport is coherent and the phonon dispersion may be tuned to reduce the phonon group velocity, leading to low thermal conductivity. This class of designs cannot be

TABLE II. Complex superlattice unit cell designs and their cross-plane thermal conductivities. All of these structures have a mass ratio of 2. Note that a shortened notation is introduced for some of the complex designs. With this notation, the  $(1 \times 1)_2 \times 2 \times 2$  superlattice is identical to the  $(1 \times 1 \times 1 \times 1 \times 2 \times 2)$  superlattice. For comparison, the thermal conductivity of an alloy with equal amounts of  $A$  and  $B$  ( $R_s = 0.5$ ) is  $0.162 \text{ W/m K}$ .

	Label	Unit Cell Design	$L$ (monolayers)	$R_s$	$k_{\text{CP}}$ (W/m K)
Class I	I	$1 \times 2 \times 2 \times 1 \times 1 \times 3$	10	0.400	0.191
	II	$2 \times 1 \times 3 \times 3 \times 2 \times 3$	14	0.500	0.199
	III	$2 \times 3 \times 1 \times 3 \times 2 \times 1 \times 1 \times 1 \times 3 \times 1$	18	0.500	0.204
Class II	IV	$1 \times 1 \times 2 \times 2$	6	0.500	0.171
	V	$1 \times 1 \times (2 \times 2)_2$	10	0.500	0.171
	VI	$1 \times 1 \times (2 \times 2)_3$	14	0.500	0.167
	VII	$1 \times 1 \times (2 \times 2)_4$	18	0.500	0.163
	VIII	$(1 \times 1)_2 \times 2 \times 2$	8	0.500	0.174
	IX	$1 \times 1 \times 1 \times 2 \times 1 \times 2$	8	0.375	0.179
	X	$1 \times 1 \times 2 \times 1 \times 2 \times 1$	8	0.625	0.168
	XI	$(1 \times 1)_3 \times 2 \times 2$	10	0.500	0.164
	XII	$(1 \times 1)_5 \times 2 \times 2$	14	0.500	0.180

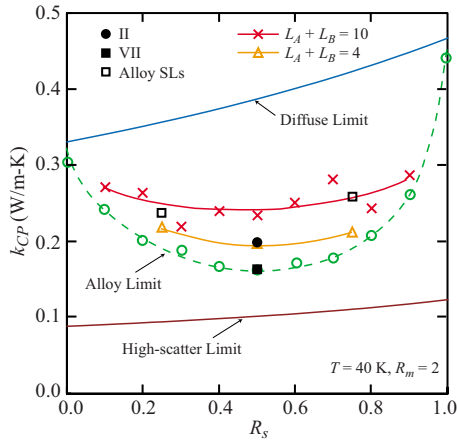


FIG. 9. (Color online) Cross-plane thermal conductivity design space for the  $R_m=2$  superlattices. The complex unit cell designs are defined in Table II.

examined here, however, because the transition between the regimes of coherent to incoherent phonon transport, which provides an estimate for the mean free path, occurs at a small total period length, leaving little room for design.

The results for some of these superlattices are plotted against the sample species ratio ( $R_s$ ) in Fig. 9. Note that only complex designs II and VII are plotted in Fig. 9 (the cross-plane thermal conductivities for all of the considered complex unit cell designs are provided in Table II). As with the  $L_A=L_B$  structures, the predicted cross-plane thermal conductivities are above the high-scatter limit and below the diffuse limit. The cross-plane thermal conductivities of the  $L_A+L_B=4$  and  $L_A+L_B=10$  superlattices are not strongly dependent on the ratio of  $L_A$  to  $L_B$ . The thermal conductivities of the alloy superlattices follow the trend of the  $L_A+L_B=10$  superlattices even though the alloy layers have a larger thermal resistance than the bulk  $A$  or  $B$  layers. This result is due to the reduction in the thermal boundary resistance of the superlattice interfaces (i.e., the acoustic mismatch between the superlattice species is less in the alloy superlattices than in the  $A|B$  superlattices). Complex design II has a cross-plane thermal conductivity of 0.199 W/m K, a value that is within the measurement uncertainty of the value for the  $2\times 2$  superlattice (0.197 W/m K). Complex design VII, however, has a cross-plane thermal conductivity of 0.163 W/m K, which is a value that is in the vicinity of the alloy limit and is  $\sim 17\%$  less than that of the minimum that is observed for the  $L_A=L_B$  superlattices.

From the results shown in Table II, we find that disordered, multilayer unit cells with lengths larger than the phonon mean free path (complex designs I–III) are not effective in reducing the cross-plane thermal conductivity below the value for the  $2\times 2$  superlattice. Our results indicate, however, that the complex designs with unit cells that are  $1\times 1$  or  $2\times 2$  superlattices with disruptions (complex designs IV–XII) all have cross-plane thermal conductivities below the value for the  $2\times 2$  superlattice. None of these designs, however, have a thermal conductivity below the alloy limit. We note that due to measurement uncertainty we cannot resolve any clear trend in the cross-plane thermal conductivity within complex designs IV–XII.

We attribute the low thermal conductivities observed for complex designs IV–XII to reductions in both the phonon group velocities and the phonon mean free paths in the regime where the phonon transport has both coherent and incoherent qualities. Because the phonon transport is coherent in the  $1\times 1$  and  $2\times 2$  superlattices, the phonon group velocities are reduced compared to those of the bulk materials.<sup>18,19,21,22,24</sup> The thermal conductivity is then further reduced by adding disruptions to these structures. These disruptions decrease the phonon mean free path below the value that would exist for the normal  $1\times 1$  and  $2\times 2$  superlattices while maintaining the low group velocities associated with those structures.

### VII. SUMMARY AND CONCLUSIONS

The Green–Kubo and direct methods were used with molecular dynamics simulations to predict the thermal conductivity of Lennard-Jones superlattices. A comprehensive comparison of the two prediction methods was provided for superlattices with two layers of equal thickness in the unit cell (i.e.,  $L_A=L_B$  structures), the first such comparison for nanocomposites. The predictions of the cross-plane thermal conductivities for these superlattices were found to be in agreement with each other to within the prediction uncertainties (see Fig. 5). After considering the uncertainties in the thermal conductivity prediction methods and the challenges encountered when applying the Green–Kubo method to more complex unit cell designs (e.g., obtaining convergence of the cross-plane HCACF integral), we decided to use the direct method for all predictions of the cross-plane thermal conductivity. The Green–Kubo method was used for all predictions of the in-plane thermal conductivity, for which application of the direct method is impractical.

The link between the superlattice unit cell design and the thermal conductivity tensor was then explored in Sec. VI. For the  $L_A=L_B$  superlattices, a minimum is predicted in the cross-plane thermal conductivity for superlattices with period lengths corresponding to the transition between coherent and incoherent phonon transport regimes. This finding is in agreement with previous theoretical predictions and some experimental observations. A maximum in the in-plane to cross-plane thermal conductivity ratio was also observed near this transition. Complex unit cell designs (characterized by having more than two layers in the unit cell) were explored to see if the cross-plane thermal conductivity could be reduced below the minimum observed for the  $L_A=L_B$  superlattices. Two different classes of complex unit cell designs were considered. In the first class, the unit cell contains many layers with no ordered subcells and has a total length greater than the phonon mean free path. These designs were found to be ineffective in reducing the cross-plane thermal conductivity. In the second class of complex designs, the unit cell contained  $1\times 1$  or  $2\times 2$  subcells with disruptions spaced on the order of the phonon mean free path. Several of these complex designs were found to have cross-plane thermal conductivities as low as the alloy limit, 17% below the minimum value for the  $L_A=L_B$  superlattices.

Our findings provide motivation for the experimental fabrication of superlattices with potentially very low thermal

conductivity, which is required in thermoelectric applications. We note that experimental measurements of strain-symmetrized, (111)-oriented Si/Ge  $L_{\text{Si}}=L_{\text{Ge}}$  superlattices indicate that phonon transport is coherent in superlattices with period lengths less than 7 nm ( $\sim 50$  monolayers).<sup>2</sup> We therefore suggest that a reduction in the cross-plane thermal conductivity may be achieved by adding disruptions of the type discussed in Sec. VI C to superlattices with layer thicknesses of 2–4 nm, which is achievable with current fabrication technology.

### ACKNOWLEDGMENTS

This work was supported by the Berkman Faculty Development Fund at Carnegie Mellon University.

### APPENDIX: IDENTIFICATION AND PREDICTION OF THE STRONG OSCILLATIONS IN THE HEAT CURRENT AUTOCORRELATION FUNCTION

Strong oscillations exist in the superlattice HCACF when the heat current definition given by Eq. (6) is applied. The cross-plane HCACF for the  $R_m=2$ ,  $3 \times 3$  superlattice is shown in the inset of Fig. 10(a) as an example. Similar oscillations have been observed in studies of diamond-structured materials,<sup>39</sup> monolayer superlattices,<sup>30</sup> complex silica structures,<sup>43</sup> metal organic framework-5,<sup>40</sup> germanium clathrate structures,<sup>41</sup>  $\text{CaF}_2$  and  $\text{UO}_2$ ,<sup>42</sup> and carbon nanotubes.<sup>44</sup> We previously suggested that these oscillations are related to zero-wave-vector optical phonon modes.<sup>30</sup> Here, we derive and test a criterion based in lattice dynamics calculations that can predict the specific phonon modes that create these oscillations.

Applying the product rule to Eq. (4) leads to

$$\mathbf{S}_1 = \sum_i \frac{d\mathbf{r}_i}{dt} E_i + \sum_i \mathbf{r}_i \frac{dE_i}{dt}. \quad (\text{A1})$$

By defining the first and second terms on the right hand side of Eq. (A1) as  $\mathbf{S}_u(t)$  and  $\mathbf{S}_k(t)$ , the HCACF can be written as

$$\begin{aligned} \langle \mathbf{S}_1(t) \cdot \mathbf{S}_1(0) \rangle &= \langle \mathbf{S}_k(t) \cdot \mathbf{S}_k(0) \rangle + 2\langle \mathbf{S}_k(t) \cdot \mathbf{S}_u(0) \rangle \\ &+ \langle \mathbf{S}_u(t) \cdot \mathbf{S}_u(0) \rangle, \end{aligned} \quad (\text{A2})$$

where there are individual contributions to the HCACF resulting from  $\mathbf{S}_u(t)$ ,  $\mathbf{S}_k(t)$ , and their cross terms. The power spectrum of the Fourier transform of these quantities is shown in Fig. 10(a) for the  $R_m=2$ ,  $3 \times 3$  superlattice (the same structure whose HCACF is shown in the inset). It is clear that the oscillations in the HCACF are primarily due to the autocorrelation of the  $\mathbf{S}_u(t)$  term.

In a solid, the position of an atom can be written as

$$\mathbf{r}_i(t) = \mathbf{r}_{i,0} + \mathbf{u}_i(t), \quad (\text{A3})$$

where  $\mathbf{u}_i(t)$  is the displacement from the equilibrium position. Under the harmonic approximation (an approximation that is exact at zero temperature),  $\mathbf{u}_i(t)$  is given by<sup>61</sup>

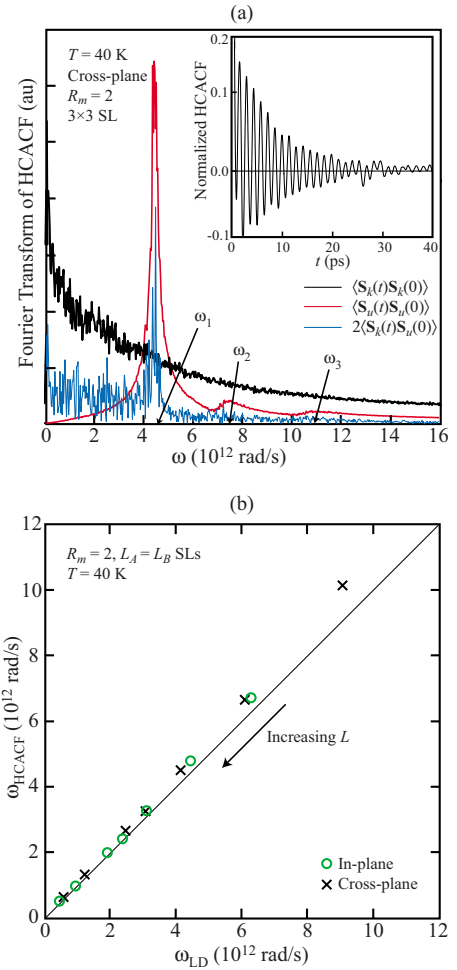


FIG. 10. (Color online) (a) Inset: Cross-plane HCACF for the  $R_m=2$ ,  $3 \times 3$  superlattice obtained using the definition of the heat current given by Eq. (4). Body: Power spectrum of the Fourier transform of the decomposed HCACF [see Eq. (A3)] shown in the inset. (b) Primary peak in the HCACF plotted against the peak predicted from the lattice-dynamics calculation for all of the  $L_A=L_B$  superlattices in both the in-plane and cross-plane directions.

$$\mathbf{u}_i(t) = \sum_{\mathbf{\kappa}, \nu} \frac{\mathbf{e}_j(\mathbf{\kappa}, \nu) \tilde{Q}(\mathbf{\kappa}, \nu, t)}{(Nm_j)^{1/2}} \exp[i(\mathbf{\kappa} \cdot \mathbf{r}_{ji})]. \quad (\text{A4})$$

Here, the summation is over all phonon normal modes and polarizations,  $N$  is the number of atoms in the system, atom  $i$  is the  $j$ th atom in the  $l$ th unit cell,  $\mathbf{\kappa}$ ,  $\nu$ , and  $\mathbf{e}$  are the phonon wave vector, dispersion branch, and polarization vector, and  $\tilde{Q}(\mathbf{\kappa}, \nu, t)$  is the normal mode coordinate, which is given by<sup>37</sup>

$$\tilde{Q}(\mathbf{\kappa}, \nu, t) = Q(\mathbf{\kappa}, \nu) \exp[-i\omega(\mathbf{\kappa}, \nu)t], \quad (\text{A5})$$

where  $Q(\mathbf{\kappa}, \nu)$  and  $\omega(\mathbf{\kappa}, \nu)$  are the phonon normal mode amplitude and frequency. Equations (A3) and (A4) can be used with the definition of  $\mathbf{S}_u(t)$  to obtain

$$\mathbf{S}_u(t) = \sum_{\boldsymbol{\kappa}, \nu} \sum_{j,l} \frac{E_{jl} \mathbf{e}_j(\boldsymbol{\kappa}, \nu)}{(Nm_j)^{1/2}} \frac{d\tilde{Q}(\boldsymbol{\kappa}, \nu, t)}{dt} \exp[i(\boldsymbol{\kappa} \cdot \mathbf{r}_{jl})], \quad (\text{A6})$$

where the summations are over all atoms, phonon normal modes, and phonon polarizations. Because

$$\sum_l \exp[i(\boldsymbol{\kappa} \cdot \mathbf{r}_{jl})] = 0 \quad (\text{A7})$$

for all phonon modes with nonzero wave vector, only phonon modes with zero wave vector will significantly contribute to the summation in Eq. (A6). Therefore, Eq. (A6) can be approximated as

$$\mathbf{S}_u(t) \approx \sum_{\nu} \sum_j \frac{n \bar{E}_j \mathbf{e}_j(\nu)}{(Nm_j)^{1/2}} \frac{d\tilde{Q}(\nu, t)}{dt}, \quad (\text{A8})$$

where the dependence on  $\boldsymbol{\kappa}$  has been dropped because we are now only referring to modes with zero wave vector,  $\bar{E}_j$  is the average energy of all of the  $j$ th atoms in each unit cell, and  $n$  is the number of unit cells.

Substituting the time derivative of Eq. (A5) into Eq. (A8) and taking the autocorrelation of the result gives

$$\langle \mathbf{S}_u(t) \cdot \mathbf{S}_u(0) \rangle = \frac{n^2}{N} \sum_{\nu} \omega^2(\nu) Q^2(\nu) \left[ \sum_j \frac{\bar{E}_j \mathbf{e}_j(\nu)}{m_j^{1/2}} \right]^2 \cos[\omega(\nu)t]. \quad (\text{A9})$$

For a classical system, the expectation value of the square of the phonon normal mode coordinate is<sup>61</sup>

$$\langle |\tilde{Q}(\boldsymbol{\kappa}, \nu, t)|^2 \rangle = \frac{k_B T}{\omega^2(\nu)}. \quad (\text{A10})$$

This quantity is a factor of 2 smaller than the square of the phonon normal mode amplitude, i.e.,

$$Q^2(\nu) = \frac{\langle |\tilde{Q}(\boldsymbol{\kappa}, \nu, t)|^2 \rangle}{2}. \quad (\text{A11})$$

Combining Eqs. (A9)–(A11) gives

$$\langle \mathbf{S}_u(t) \cdot \mathbf{S}_u(0) \rangle = \frac{k_B T n^2}{N} \sum_{\nu} \left[ \sum_j \frac{\bar{E}_j \mathbf{e}_j(\nu)}{m_j^{1/2}} \right]^2 \cos[\omega(\nu)t]. \quad (\text{A12})$$

Equation (A12) is a sum of oscillatory functions corresponding to optical phonon modes with zero wave vector. The

summation over  $j$  can be used as a criterion for when a peak should exist in the Fourier transform of the HCACF. That is, when

$$\left[ \sum_j \frac{\bar{E}_j \mathbf{e}_j(\nu)}{m_j^{1/2}} \right]^2 \neq 0, \quad (\text{A13})$$

the Fourier transform of the HCACF will have a peak at  $\omega(\nu)$ . The relative peak amplitudes should also be related to the magnitude of the term on the left hand side of Eq. (A13).

By using the quasiharmonic approximation,<sup>61</sup> the zero-wave-vector phonon normal mode polarizations and frequencies have been calculated for all of the  $L_A=L_B$  superlattices, and Eq. (A13) has been evaluated to predict the frequency peaks in the Fourier transform of the HCACF. For the  $R_m=2$ ,  $3 \times 3$  superlattice, a strong peak is predicted for  $\omega_1=4.15 \times 10^{12}$  rad/s, which is a value that is 8% lower than the dominant peak frequency of  $\omega_1=4.49 \times 10^{12}$  rad/s [see Fig. 10(a)]. Two additional peaks are predicted for  $\omega_2=6.80 \times 10^{12}$  rad/s and  $\omega_3=9.77 \times 10^{12}$  rad/s. The values of the term on the left hand side of Eq. (A13) for these peaks are 16 and 31 times less than the value for the primary peak. These weak secondary and tertiary peaks can also be observed in Fig. 10(a) at frequencies of  $\omega_2=7.5 \times 10^{12}$  rad/s and  $\omega_3=10.9 \times 10^{12}$  rad/s. The primary peaks in the Fourier transform of the cross-plane and in-plane HCACFs ( $\omega_{\text{HCACF}}$ ) for all of the  $R_m=2$ ,  $L_A=L_B$  superlattices considered here are compared to values predicted by the lattice-dynamics calculation ( $\omega_{\text{LD}}$ ) in Fig. 10(b). The maximum difference between the predicted and observed peak frequencies is 11% for the  $R_m=2$ ,  $1 \times 1$  superlattice in the cross-plane direction. We believe that the source of error in the prediction is that anharmonic effects are not included in the lattice dynamics calculations. To prove this point, a simulation was run at a temperature of 10 K for the  $R_m=2$ ,  $3 \times 3$  superlattice, and the prediction accuracy of the primary cross-plane peak improved from 8% to 1%.

We note that the procedure outlined in this appendix was successful in predicting the phonon modes that lead to the oscillations in the HCACF reported for several complex silica structures.<sup>43</sup> Because all of the other studies<sup>30,39–42,44</sup> that have observed similar oscillations in the HCACF used the heat current definition given by Eq. (4), we believe that the peaks observed in those studies are also related to the autocorrelation of the  $\mathbf{S}_u(t)$  term and can be predicted by using the procedure outlined here or omitted by choosing the  $\mathbf{S}_1$  heat current definition [Eq. (5)].

\*mcgaughey@cmu.edu

<sup>1</sup>W. S. Capinski, H. J. Maris, T. Ruf, M. Cardona, K. Ploog, and D. S. Katzer, Phys. Rev. B **59**, 8105 (1999).

<sup>2</sup>S. Chakraborty, C. A. Kleint, A. Heinrich, C. M. Schneider, J. Schumann, M. Falke, and S. Teichert, Appl. Phys. Lett. **83**, 4184 (2003).

<sup>3</sup>J. C. Caylor, K. Coonley, J. Stuart, T. Colpitts, and R. Venkatasubramanian, Appl. Phys. Lett. **87**, 023105 (2005).

<sup>4</sup>Y. Ezzahri, S. Dilhaire, S. Grauby, J. M. Rampnoux, W. Claeys, Y. Zhang, G. Zeng, and A. Shakouri, Appl. Phys. Lett. **87**, 103506 (2005).

<sup>5</sup>T. Borca-Tasciuc *et al.*, Superlattices Microstruct. **28**, 199

- (2000).
- <sup>6</sup>T. Borca-Tasciuc *et al.*, *J. Appl. Phys.* **92**, 4994 (2002).
  - <sup>7</sup>S. T. Huxtable, A. R. Abramson, C.-L. Tien, A. Majumdar, C. LaBounty, X. Fan, G. Zeng, J. E. Bowers, A. Shakouri, and E. T. Croke, *Appl. Phys. Lett.* **80**, 1737 (2002).
  - <sup>8</sup>R. Venkatasubramanian, *Phys. Rev. B* **61**, 3091 (2000).
  - <sup>9</sup>B. Yang, W. L. Liu, J. L. Liu, K. L. Wang, and G. Chen, *Appl. Phys. Lett.* **81**, 3588 (2002).
  - <sup>10</sup>A. Mavrokefalos, *Appl. Phys. Lett.* **91**, 171912 (2007).
  - <sup>11</sup>C. Chiritescu, D. G. Cahill, N. Nguyen, D. Johnson, A. Bodapati, P. Keblinski, and P. Zschack, *Science* **315**, 351 (2007).
  - <sup>12</sup>G. Chen, M. S. Dresselhaus, G. Dresselhaus, J.-P. Fleurial, and T. Caillat, *Int. Mater. Rev.* **48**, 45 (2003).
  - <sup>13</sup>H. Bottner, G. Chen, and R. Venkatasubramanian, *MRS Bull.* **31**, 211 (2006).
  - <sup>14</sup>W. Kim, J. Zide, A. Gossard, D. Klenov, S. Stemmer, A. Shakouri, and A. Majumdar, *Phys. Rev. Lett.* **96**, 045901 (2006).
  - <sup>15</sup>W. Kim, R. Wang, and A. Majumdar, *Nanotoday* **2**, 40 (2007).
  - <sup>16</sup>M. V. Simkin and G. D. Mahan, *Phys. Rev. Lett.* **84**, 927 (2000).
  - <sup>17</sup>B. Yang and G. Chen, *Phys. Rev. B* **67**, 195311 (2003).
  - <sup>18</sup>D. A. Broido and T. L. Reinecke, *Phys. Rev. B* **70**, 081310(R) (2004).
  - <sup>19</sup>B. Yang and G. Chen, *Microscale Thermophys. Eng.* **5**, 107 (2001).
  - <sup>20</sup>S. F. Ren, W. Cheng, and G. Chen, *Microelectron. J.* **100**, 103505 (2006).
  - <sup>21</sup>S. I. Tamura, Y. Tanaka, and H. J. Maris, *Phys. Rev. B* **60**, 2627 (1999).
  - <sup>22</sup>A. A. Kiselev, K. W. Kim, and M. A. Stroschio, *Phys. Rev. B* **62**, 6896 (2000).
  - <sup>23</sup>P. Hyldgaard and G. D. Mahan, *Phys. Rev. B* **56**, 10754 (1997).
  - <sup>24</sup>W. E. Bies, R. J. Radtke, and H. Ehrenreich, *J. Appl. Phys.* **88**, 1498 (2000).
  - <sup>25</sup>A. R. Abramson, C.-L. Tien, and A. Majumdar, *J. Heat Transfer* **124**, 963 (2002).
  - <sup>26</sup>Y. Chen, D. Li, J. R. Lukes, Z. Ni, and M. Chen, *Phys. Rev. B* **72**, 174302 (2005).
  - <sup>27</sup>B. C. Daly, H. J. Maris, K. Imamura, and S. Tamura, *Phys. Rev. B* **66**, 024301 (2002).
  - <sup>28</sup>K. Imamura, Y. Tanaka, N. Nishiguchi, S. Tamura, and H. J. Maris, *J. Phys.: Condens. Matter* **15**, 8679 (2003).
  - <sup>29</sup>S. Volz, J. B. Saulnier, G. Chen, and P. Beauchamp, *Microelectron. J.* **31**, 815 (2000).
  - <sup>30</sup>A. J. H. McGaughey, M. I. Hussein, E. S. Landry, M. Kaviani, and G. M. Hulbert, *Phys. Rev. B* **74**, 104304 (2006).
  - <sup>31</sup>B. C. Daly, H. J. Maris, Y. Tanaka, and S. Tamura, *Phys. Rev. B* **67**, 033308 (2003).
  - <sup>32</sup>P. K. Schelling, S. R. Phillpot, and P. Keblinski, *Phys. Rev. B* **65**, 144306 (2002).
  - <sup>33</sup>N. W. Ashcroft and N. D. Mermin, *Solid State Physics* (Saunders, Fort Worth, 1976).
  - <sup>34</sup>A. J. H. McGaughey, Ph.D. thesis, University of Michigan, 2004.
  - <sup>35</sup>D. A. McQuarrie, *Statistical Mechanics* (University Science Books, Sausalito, 2000).
  - <sup>36</sup>A. J. H. McGaughey and M. Kaviani, in *Advances in Heat Transfer*, edited by G. A. Greene, Y. I. Cho, J. P. Hartnett, and A. Bar-Cohen (Elsevier, New York, 2006), Vol. 39, pp. 169–255.
  - <sup>37</sup>A. J. C. Ladd, B. Moran, and W. G. Hoover, *Phys. Rev. B* **34**, 5058 (1986).
  - <sup>38</sup>J. Li, Ph.D. thesis, Massachusetts Institute of Technology, 2000.
  - <sup>39</sup>J. Che, T. Cagin, W. Deng, and W. A. Goddard III, *J. Chem. Phys.* **113**, 6888 (2000).
  - <sup>40</sup>B. L. Huang, A. J. H. McGaughey, and M. Kaviani, *Int. J. Heat Mass Transfer* **50**, 393 (2007).
  - <sup>41</sup>J. Dong, O. F. Sankey, and C. W. Myles, *Phys. Rev. Lett.* **86**, 2361 (2001).
  - <sup>42</sup>P. J. D. Lindan and M. J. Gillan, *J. Phys.: Condens. Matter* **3**, 3929 (1991).
  - <sup>43</sup>A. J. H. McGaughey and M. Kaviani, *Int. J. Heat Mass Transfer* **47**, 1799 (2004).
  - <sup>44</sup>Z. Yao, J.-S. Wang, B. Li, and G.-R. Liu, *Phys. Rev. B* **71**, 085417 (2005).
  - <sup>45</sup>A. J. H. McGaughey and M. Kaviani, *Int. J. Heat Mass Transfer* **47**, 1783 (2004).
  - <sup>46</sup>H. Kaburaki, J. Li, S. Yip, and H. Kimizuka, *J. Appl. Phys.* **102**, 043514 (2007).
  - <sup>47</sup>E. T. Swartz and R. O. Pohl, *Rev. Mod. Phys.* **61**, 605 (1989).
  - <sup>48</sup>J. Che, T. Cagin, and W. A. Goddard III, *Nanotechnology* **11**, 65 (2000).
  - <sup>49</sup>J. R. Lukes, D. Y. Li, X.-G. Liang, and C.-L. Tien, *J. Heat Transfer* **122**, 536 (2000).
  - <sup>50</sup>E. S. Landry, A. J. H. McGaughey, and M. I. Hussein, *Proceedings of the HT 2007* (ASME, New York, 2007), Paper No. HT2007-32152.
  - <sup>51</sup>E. S. Landry, A. J. H. McGaughey, and M. I. Hussein, *Proceedings of the IMECE 2007* (ASME, New York, 2007), Paper No. IMECE2007-43177.
  - <sup>52</sup>T. Ikeshoji and B. Hafskjold, *Mol. Phys.* **81**, 251 (1994).
  - <sup>53</sup>F. P. Incropera and D. P. DeWitt, *Fundamentals of Heat and Mass Transfer* (Wiley, Hoboken, NJ, 2002).
  - <sup>54</sup>Y. Chen, D. Li, J. Yang, Y. Wu, J. R. Lukes, and A. Majumdar, *Physica B (Amsterdam)* **349**, 270 (2004).
  - <sup>55</sup>A. J. H. McGaughey and M. Kaviani, *Phys. Rev. B* **71**, 184305 (2005).
  - <sup>56</sup>P. Heino, *J. Comput. Theor. Nanosci.* **4**, 896 (2007).
  - <sup>57</sup>D. G. Cahill, S. K. Watson, and R. O. Pohl, *Phys. Rev. B* **46**, 6131 (1992).
  - <sup>58</sup>M. G. Holland, *Phys. Rev.* **132**, 2461 (1963).
  - <sup>59</sup>D. J. Paul, *Semicond. Sci. Technol.* **19**, R75 (2004).
  - <sup>60</sup>M. I. Hussein, K. Hamza, G. M. Hulbert, and K. Saitou, *Struct. Multidiscip. Optim.* **31**, 60 (2006).
  - <sup>61</sup>M. T. Dove, *Introduction to Lattice Dynamics* (Cambridge University Press, Cambridge, 1993).